Microwave assisted crystalline and morphology evolution of flower-like Fe2O3@ iron doped K-birnessite composite and its application for lithium ion storage

Huang, Wei; Zheng, Xiaowen; Shangguan, Huihui; Xiao, Xinxin; Tang, Jing; Sun, Hongyu; Mølhave, Kristian; Ci, Lijie; Si, Pengchao; Zhang, Jingdong

Published in:
Applied Surface Science

Link to article, DOI:
10.1016/j.apsusc.2020.146513

Publication date:
2020

Document Version
Peer reviewed version

Cite this paper: Wei Huang, Xiaowen Zheng, Huihui Shangguan, **Xinxin Xiao**, Jing Tang, Hongyu Sun, Kristian Mølhave, Lijie Ci, Pengchao Si and Jingdong Zhang; Microwave assisted crystalline and morphology evolution of flower-like Fe_2O_3@ iron doped K-birnessite composite and its application for lithium ion storage, ***Applied Surface Science*** 2020, DOI: 10.1016/j.apsusc.2020.146513

Microwave assisted crystalline and morphology evolution of flower-like Fe_2O_3@ iron doped K-birnessite composite and its application for lithium ion storage

Wei Huang,[a] Xiaowen Zheng,[b] Huihui Shangguan,[b] Xinxin Xiao,[a] Jing Tang,[a] Hongyu Sun,[c] Kristian Mølhave,[c] Lijie Ci,[b] Pengchao Si [b, *] and Jingdong Zhang [a, **]

[a] *Department of Chemistry, Technical University of Denmark, DK-2800 Kongens Lyngby, Denmark.*

[b] *SDU & Rice Joint Center for Carbon Nanomaterials, Key Laboratory for Liquid-Solid Structural Evolution and Processing of Materials, Ministry of Education, School of Materials Science and Engineering, Shandong University, Jinan 250061, P. R. China.*

[c] *DTU Nanolab - National Center for Nanofabrication and Characterization, Technical University of Denmark, DK-2800 Kongens Lyngby, Denmark.*

* *Corresponding author: pcsi@sdu.edu.cn (Pengchao Si).*

** *Corresponding author: jz@kemi.dtu.dk (Jingdong Zhang).*

ABSTRACT: Manganese oxides (MnO_x) and derivations are considered as one of the most attractive anode materials for lithium-ion batteries (LIBs) due to their earth-abundant, cost-effective and low-toxic specialties. Herein, we report a flower-like composite consisting of internal Fe_2O_3 nanocrystals and outer hierarchal iron doped K-birnessite type MnO_x layers (Fe_2O_3@Fe doped K-birnessite), which is synthesized by a facile one-pot microwave-assisted heating synthesis (MAHS). The crystalline and morphology evolution of Fe_2O_3@Fe doped K-birnessite composite are studied by checking the products at various reaction durations, using X-ray diffraction (XRD), X-ray photoelectron spectroscopy (XPS) and scanning & transmission electron microscopy (SEM & TEM). Key factors affecting the morphology such as reactive temperature and stoichiometric ratio are systematically investigated. When tested for LIBs, the optimized hybrid Fe_2O_3@Fe doped K-birnessite composite exhibits a high reversible capacity of 758 mA h g^{-1} at 500 mA g^{-1} after 200 cycles, outperforming the pure K-birnessite (203 mA h g^{-1}). The excellent electrochemical performance is assigned to the efficient utilization of the merits of the flower-like structure and strong interaction between MnO_x and Fe_2O_3. Further, crucial factors associated with structural stability of Fe_2O_3@Fe doped K-birnessite composite during cycling are identified.

Keywords: Fe_2O_3; iron doped K-birnessite; crystalline evolution; morphology evolution; lithium ion storage.

1. Introduction

Rechargeable lithium-ion batteries (LIBs) represent one of the most appealing and widely used clean energy storage technologies [1, 2]. However, the relatively low theoretical specific capacity of graphite (372 mA h g^{-1}) based anodes for LIBs could hardly meet the urgent demand for large-scale electronic devices [3]. The development of the next-generation anode materials for superior rechargeable LIBs with high electrochemical capacities and minimal environmental hazard is crucial [4-9]. Transition metal oxides (TMOs) exhibit significant theoretical capacities based on a typical conversion-type reaction ($MO_x + 2x\ Li^+ + 2x\ e^- \leftrightarrow M + x\ Li_2O$), which are typically more than twice of that of graphite with the insertion mechanism for lithium ion storage [10-15]. Among various TMO-based materials, manganese oxides (MnO_x) have attracted numerous interests for anode materials due to the earth-abundant, cost-effective and low-toxic features [16-18]. MnO_x displays a lower lithium ion inserting potential (0.2 V vs. Li/Li^+) than those of other TMOs, which could provide wider voltage range [19]. However, similar to other TMOs, MnO_x suffers from low electrical conductivity and a rapid capacity attenuation due to the volume expansion during lithium insertion/extraction.

To cope with the aforementioned challenge, one approach is to fabricate different nanostructured MnO_x, such as Mn_3O_4 nanoparticle [20], Mn_3O_4 nanofiber [21], nanocrystalline MnO thin film[22] etc. However, the low electrical conductivity and high surface energy of MnO_x nanomaterials lead to the drastic capacity decay (Table S1). Another method is to combine MnO_x with conductive carbonaceous materials (graphene [23, 24], carbon nanotube [25]), which could accommodate large volume change and promote the electrical conductivity for high lithium storage capacity. Alternatively, the incorporation of MnO_x with other transition metal based components emerges as a cost-efficient way to promote the lithium storage performance [26-29]. For example, Svensson et al. have reported $Co(OH)_2$@MnO_2 nanosheet arrays as binder-free electrodes through a two-step process consisting of electrodeposition and heating [28]. The hybrids displayed a reasonable lithium storage capacity of 420 mA h g^{-1} at 1000 mA g^{-1} after 500 cycles, ascribed to the synergetic effects from the stable structure of $Co(OH)_2$ and MnO_2 [28]. Xiao and co-workers have fabricated Fe_2O_3@amorphous MnO_2 composites for enhanced lithium storage through sequential synthetic methods including solution-phase reaction, annealing and hydrothermal reaction, which exhibited a capacity of 555 mA h g^{-1} at 1000 mA g^{-1} after 100 cycles. The enhanced lithium storage performance is due to that the assembled amorphous MnO_2 nanosheets were *in situ* transformed into a Fe-Mn-O protection layer for better electrical conductivity and enhanced structural integration [29]. It has been demonstrated that introduction of the doping of other metal elements in the MnO_x could effectively improve the physicochemical properties of MnO_x with good electrochemical performance [30-33]. For example, Komaba and coworkers have reported different metal (Al, Ni or Co) dopings in K-birnessite-type manganese dioxides

for enhanced lithium storage by longstanding solution-phase reaction and annealing [32]. Lee et al. have synthesized Fe-doped Mn_xO_y with hierarchical porous structure through a combined strategy of solution-phase reaction and annealing, showing a high-performance lithium capacity of 620 mA h g^{-1} at 200 mA g^{-1} after 100 cycles. The doping metal elements in the MnO_x improve the bulk conductivity and local electron transfer kinetics [33]. However, most of the previous reports require long-standing and elaborate synthetic procedures. It is thus promising to develop a low-cost and simple method to construct hybrid TMOs cooperating with heteroatom doped MnO_x for high-performance LIBs.

Microwave-assisted heating synthesis (MAHS) is regarded as a facile synthetic strategy with high reaction efficiency and reduced energy consumption compared with the traditional heating methods [34-36]. It holds the potential to be scaled up for industrial applications in case issues, such as limited penetration depth of the absorbed microwaves, can be well addressed. Besides, MAHS is surfactant-free strategy which circumvents the hinderance induced by capping agents around the nanomaterials [37]. Materials obtained by surfactant-free MAHS possess great potentials for energy storage and conversion by carefully tailoring the material structure and compositions through the fine control of microwave reaction [38, 39]. For example, Li and co-workers have demonstrated MAHS-derived birnessite-type MnO_2 nanospheres for supercapacitor electrodes, exhibiting a specific capacitance of 210 F g^{-1} at 200 mA g^{-1} [38]. Wang et al. demonstrated the morphology evolution control of Fe based metal-organic frameworks by MAHS, thus optimizing the derived Fe_2O_3 nanostructures for high-performance LIBs [39]. To the best of our knowledge, there is no report on

controllably synthesizing homogeneous composites combining Fe doped birnessite-type MnO_2 with Fe_2O_3 by MAHS for enhanced lithium-ion storage performance.

Herein, flower-like Fe_2O_3@Fe doped K-birnessite composite has been successfully prepared with one-pot MAHS. The outer hierarchal iron doped K-birnessite type MnO_x layers containing internal Fe_2O_3 nanocrystals constitute into the flower-like structure, whose formation process is systematically investigated. Further, the composite shows a superior lithium-ion storage performance than pure K-birnessite, exhibiting a good lithium storage reversible capacity of 758 mA h g^{-1} at 500 mA g^{-1} after 200 cycles.

2. Experimental section

2.1. Chemicals and reagents.

Potassium permanganate ($KMnO_4$, ≥ 99.9%) was purchased from Merck (Germany). Iron (II) sulfate heptahydrate ($FeSO_4·7H_2O$, ≥ 99.0%) and manganese (II) sulfate monohydrate ($MnSO_4·H_2O$, meets USP testing specifications) were purchased from Sigma-Aldrich, Denmark. All chemicals were used as received without further purification. Ultrapure water (>18.25 MΩ·cm, Sartorius arium® pro, Germany) was used for all the aqueous solution preparation.

2.2. Synthesis of flower-like Fe_2O_3@Fe doped K-birnessite composite.

In a typical procedure, 0.200 g $KMnO_4$ and 0.100 g $FeSO_4·7H_2O$ were dissolved in 15 mL ultrapure water under stirring for 15 min to form a uniform purple solution, which was transferred to microwave reaction vials (10-20 mL, Biotage, Sweden). The vials were heated in a microwave oven (Biotage® Initiator+ Robot Eight) at 140 °C (pressure: 6 bar, power: 31 W) with different durations (30, 60, 90 and 180 min) to investigate the crystalline and morphology evolution of the Fe_2O_3@Fe doped K-birnessite composite. The obtained products

were centrifuged and washed with ultrapure water for more than three times, and then dried in an oven at 110°C for 6 h. The pure K-birnessite composite was fabricated as a control with the same procedure using 0.200 g $KMnO_4$ and 0.061 g $MnSO_4 \cdot H_2O$.

2.3. Materials characterization.

Microstructure was analyzed by using the scanning electron microscope (SEM, Quanta FEG 200 ESEM, 15 kV) and transmission electron microscope (TEM, Tecnai G2 T20, 200 kV). Crystalline specialties of composites were tested by X-ray diffraction (XRD, Miniflex 600, Cu-Kα radiation, λ = 1.5418 Å) and X-ray photoelectron spectroscopic (XPS, Thermo-Scientific system (Al-Kα radiation, 1484.6 eV) analysis, respectively. Specific surface area was recorded by a Surface Area & Pore Size Analyzer (ASAP 2020, Micromeritics). The elemental compositions analysis of sample was performed by inductively-coupled plasma optical emission spectrometry (ICP-OES).

2.4. Electrochemical performance for lithium ion storage.

Mixed active materials (70 wt%), super P (20 wt%) and polyvinylidene fluoride (PVDF, 10 wt%) were dissolved in N-methyl-2-pyrrolidone (NMP) as a slurry to coat on the copper foil. Then, the prepared electrode materials were dried in a vacuum oven at 80 °C for 12 h. The mass loading on a working electrode was about 1.4 mg. Lithium foil was used as the counter electrode. 1.0 M $LiPF_6$ dissolved in a solution composed of dimethyl carbonate, ethylene carbonate, diethyl carbonate (1:1:1 in volumetric ratio) was used as the electrolyte. Half coin cells (CR 2016) were assembled in a glove box under argon atmosphere at room temperature. Galvanostatic discharge/charge (GDC) tests in a voltage window of 0.01-3.0 V were recorded with a Neware-CT-3008 test system (Shenzhen, China). Cyclic voltammograms (CVs) in the voltage range of 0.01-3.0 V at a scan rate of 0.1 mV s^{-1} were recorded with a CHI 660E

electrochemical workstation (Shanghai, China). Electrochemical impedance spectroscopic (EIS) characterization in a frequency range of 0.01 to 100 kHz was carried out at the open circuit potential (OCP) by the Autolab instrument (Metrohm).

3. Results and discussion

3.1. Formation process and crystalline evolution with different reactive durations.

The overall formation process of synthetic materials is illustrated in Scheme 1. Firstly, $KMnO_4$ (oxidizing agent) reacts with $FeSO_4$ (reducing agent) by one-pot microwave reaction. In order to investigate the formation process of the Fe_2O_3@Fe doped K-birnessite composites, different microwave reactive durations (30, 60, 90 and 180 min) are adopted. Fig. 1a shows the X-ray diffraction (XRD) patterns of corresponded synthetic samples with a growth time of 30 and 60 min, respectively. No obvious diffraction peaks are detected, indicating the amorphous state of generated composites. When the growth time increases to 90 min, some weak peaks assigned to Hematite type Fe_2O_3 (JCPDS no. 33-0664) are observed. When the growth time is up to 180 min, distinct diffraction peaks match well with birnessite (JCPDS no. 80-1098) and some slight peaks are allocated to Fe_2O_3 (JCPDS no. 33-0664). The related diffraction peaks (Fig. S1) are distinguished in detail, with all recognizable peaks assigned to the corresponding crystalline planes of K-birnessite and Fe_2O_3. Besides, the XRD patterns of synthetic samples with 360 min growth time (Fig. S2) are similar to those obtained with 180 min, indicative of the stable existence of synthetic composite after 180 min microwave reaction. As a control, the pure K-birnessite composite with 180 min growth time (Fig. S3) is also detected, showing a typical birnessite crystalline structure (JCPDS no. 80-1098). In addition, the surface elemental chemical states of synthetic samples with different growth times (30, 60, 90 and 180 min) are characterized by using X-ray photoelectron spectroscopy

(XPS). The XPS spectra (Fig. S4) of 30, 60 and 90 min clearly show the existences of Fe, Mn and O elements on the surface of synthetic samples. High-resolution Fe 2p spectrum (Fig. 1b) of 30 min located at 712.5 (Fe $2p_{3/2}$) and 725.8 eV (Fe $2p_{1/2}$) indicate the presence of Fe^{3+} originating from FeOOH, which is in agreement with previous reports [40]. When the growth time increases to 60 or 90 min, the peaks in high-resolution Fe 2p spectrum shift to lower binding energies, which are assigned to the Fe^{3+} of Fe_2O_3 due to the decomposition of FeOOH [41]. When the growth time is up to 180 min, high-resolution Fe 2p spectrum (Fig. 1b) shows a weak signal, indicating the presence of small amounts of Fe^{3+} on the surface of Fe_2O_3@Fe doped K-birnessite composite. As a control, the XPS spectra of pure K-birnessite composite have been also detected (Fig. S5), exhibiting the elemental Mn, O and K signals. The high-resolution Mn 2p spectra are shown in Fig. 1c, the binding energy of Mn $2p_{3/2}$ for pure K-birnessite is 642.38 eV, while it shifts to 642.57 eV with higher electron binding energy for Fe_2O_3@Fe doped K-birnessite, indicating higher state of Mn [42]. In addition, the peaks of Mn 2p spectra with Fe_2O_3@Fe doped K-birnessite (Fig. 1d) and pure K-birnessite (Fig. 1e) composites are deconvoluted into three kinds of valence states of Mn (Mn^{2+}, Mn^{3+} and Mn^{4+}). The manganese distributions (Mn $2p_{3/2}$) of Fe_2O_3/Fe doped K-birnessite for Mn^{2+}, Mn^{3+} and Mn^{4+} are 12.99%, 20.35% and 66.66%, respectively. In contrast, the manganese distributions (Mn $2p_{3/2}$) of pure K-birnessite for Mn^{2+}, Mn^{3+} and Mn^{4+} are 11.52%, 27.03% and 61.45%, respectively. The decrease of Mn^{3+} percentage content for Fe_2O_3@Fe doped K-birnessite than pure K-birnessite is attributed to the substitution of Fe^{3+} for Mn^{3+}, validating the iron doping in the Fe_2O_3@Fe doped K-birnessite composite [42, 43]. Moreover, the typical nitrogen adsorption-desorption isotherms are shown in Fig. 1f. The specific surface area of Fe_2O_3@Fe doped K-birnessite is calculated to be 241.1 $m^2 g^{-1}$, ca. 9 times of the value of pure K-birnessite (26.4 $m^2 g^{-1}$). The higher specific surface area for Fe_2O_3@Fe doped K-birnessite is the result of

the formation of finer porous structure, as well as the reduced thickness of birnessite plate crystals and the presence unfold the stacking layers due to iron doping [44]. Fe_2O_3@Fe doped K-birnessite (Fig. S6) displays a mesoporous structure (2-50 nm) with pore-size distribution centered at 46.6 nm, while pure K-birnessite (Fig. S5) shows a macroporous structure (>50 nm) whose pore size is mainly located at 85.5 nm. The finer mesoporous structure and higher specific surface area for the Fe_2O_3@Fe doped K-birnessite than the pure K-birnessite could provide more active sites for lithium ion insertion/extraction.

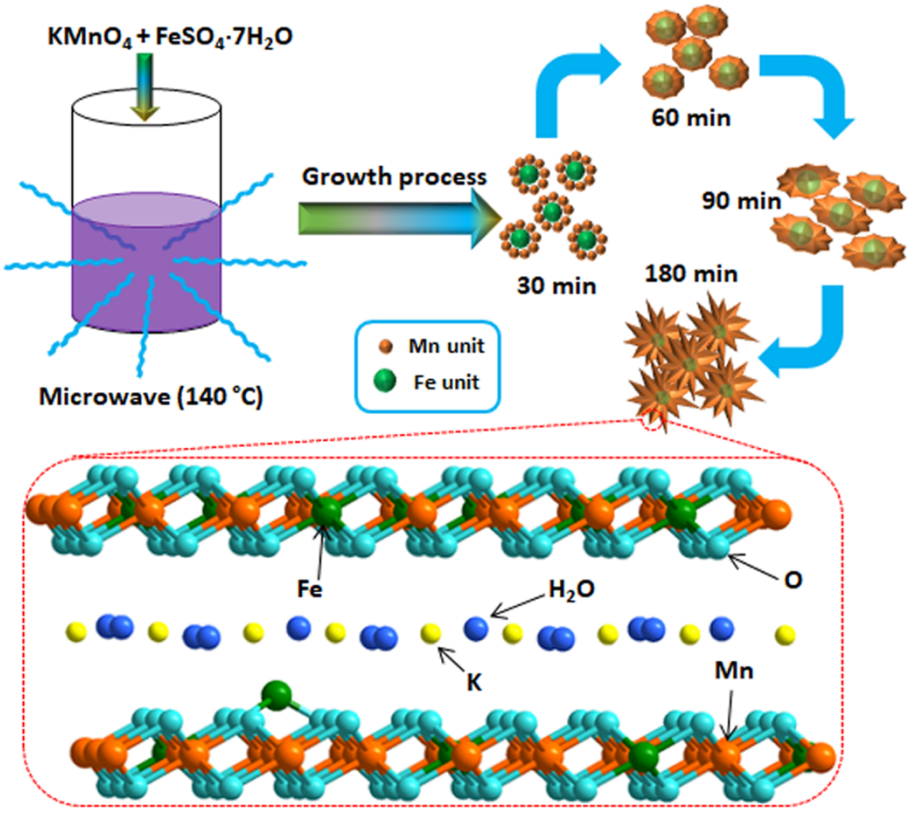

Scheme 1. Schematic illustration of the growth process of the Fe_2O_3@Fe doped K-birnessite composite. Inset shows Fe_2O_3@Fe doped K-birnessite MnO_x layers. Not drawn to real scale.

Based on the above characterization, the overall formation process involving of several chemical reactions is proposed [45, 46]. In the very beginning, $KMnO_4$ reacts with H^+ from the acidic mixed solution (pH = 2.3), decomposing into MnO_2 and O_2 in the microwave heating

process (Eq. 1). The generated O_2 oxidizes the Fe^{2+} to FeOOH (Eq. 2), which is further decomposed into Fe_2O_3 under heating (Eq. 3). Fe_2O_3 reacts with the previously generated H^+ from Eq. 2 with the formation of Fe^{3+} (Eq. 4), leading the Fe doping in the layer structure of composite. It is noteworthy that the generated H^+ is not enough to react with the entire Fe_2O_3 (Eq. 2, 4), thus the slight peaks of Fe_2O_3 (Fig. 1a) can be observed from the XRD patterns of Fe_2O_3@Fe doped K-birnessite composite. Moreover, the formative MnO_2 is further oxidized to layer-structural MnO_x (Mn^{2+}, Mn^{3+} and Mn^{4+}).

$$4\ MnO_4^- + 4\ H^+ \xrightarrow{\Delta} 4\ MnO_2 + 3\ O_2\uparrow + 2\ H_2O \quad (1)$$

$$4\ Fe^{2+} + O_2 + 6\ H_2O \rightarrow 4\ FeOOH + 8\ H^+ \quad (2)$$

$$2\ FeOOH \xrightarrow{\Delta} Fe_2O_3 + H_2O \quad (3)$$

$$Fe_2O_3 + 6\ H^+ \rightarrow 2\ Fe^{3+} + 3\ H_2O \quad (4)$$

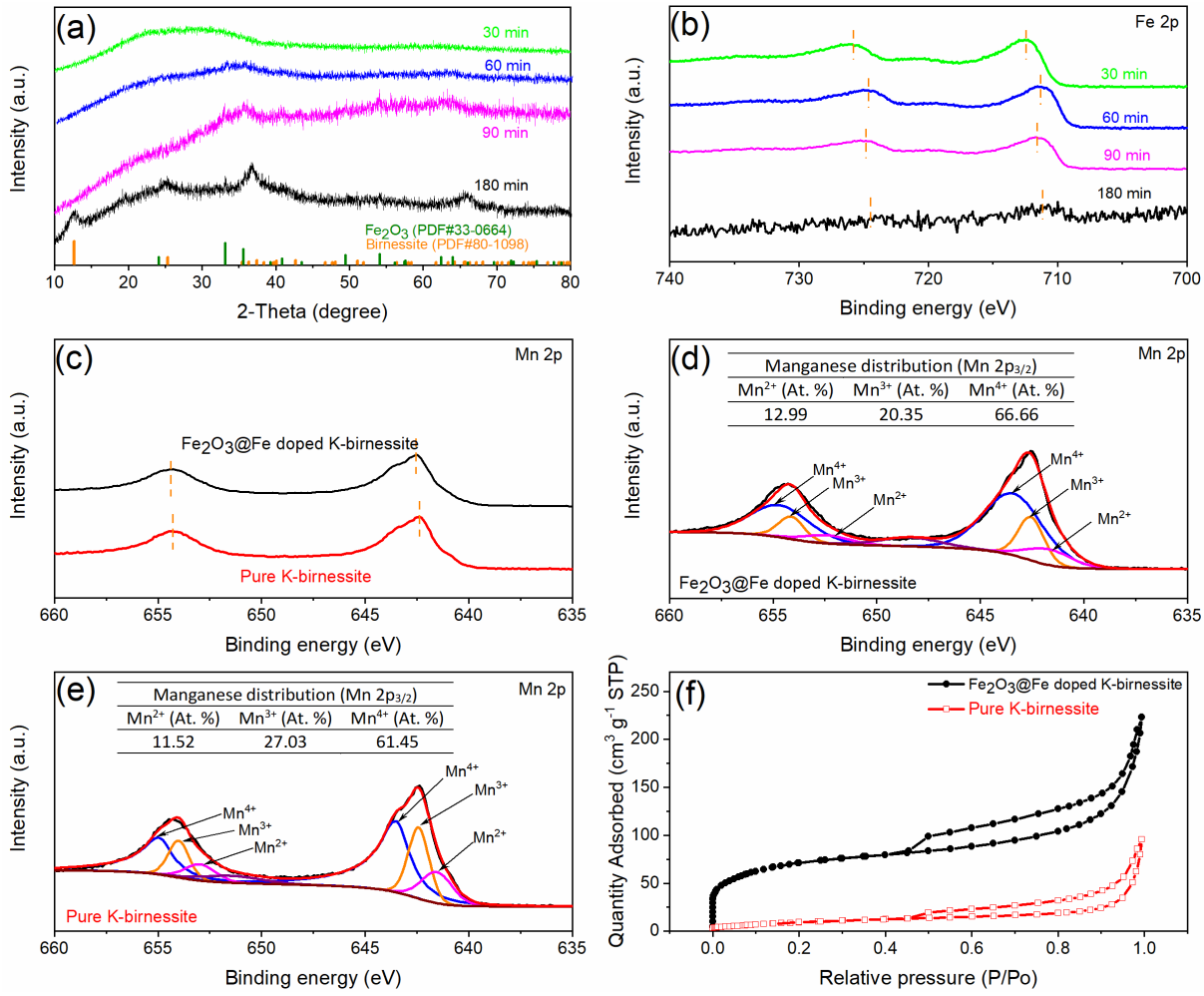

Fig. 1. (a) XRD patterns of synthetic samples with different growth durations (30, 60, 90 and 180 min). (b) High-resolution XPS spectra of Fe 2p of synthetic samples with different growth times (30, 60, 90 and 180 min). (c-e) High-resolution XPS spectra of Mn 2p of Fe_2O_3@Fe doped K-birnessite (d) and pure K-birnessite (e) composites; insets in Figure 2d and e are the manganese distribution ($Mn2p_{3/2}$). (f) Typical nitrogen adsorption-desorption isotherms of Fe_2O_3@Fe doped K-birnessite and pure K-birnessite composites.

3.2. Morphology evolution with different reactive durations.

The morphology evolution of synthetic samples with different growth times are investigated by scanning electron microscopy (SEM) and transmission electron microscopy (TEM). When the growth time is 30 min, the generated samples (Fig. 2a, e and i) show a

uniform spherical shape. This is attributed to a rapid nucleation of high concentrations of Mn and Fe sources in the beginning, a process that a large amount of formative small nuclei aggregated into the spherical morphology with minimized surface energy [47]. As the growth time increases to 60 min, the generated small particles (Fig. 2b, f and j) gradually grow up and stack together into a spherical nanoplate shape. For 90 min, the stacked spherical nanoplates (Fig. 2c, g and k) further grow up and become thicker. When the growth time is 180 min, the generated Fe_2O_3@Fe doped K-birnessite composite shows a homogenous flower-like structure. The formation of MnO_x sheets on the edge of the composite is mainly due to the abundant positive cations (K^+, Fe^{3+}) or H_2O molecules which effectively maintain the stability of layer structure [48]. Besides, the samples of 360 min (Fig. S7) show similar flower-like structure of 180 min, implying the stable Fe_2O_3@Fe doped K-birnessite composite. As a control, SEM images of synthetic pure K-birnessite composites with growth durations of 30 (Fig. S8a-c), 60 (Fig. S8d-f), 90 (Fig. S8g-i) and 180 (Fig. S8j-l) min show similar thick uneven hierarchical structure. There are no significant differences between those samples in terms of morphology, indicating of a quick completion of the reaction within 30 min. This is because the presence of high concentrated MnO_4^- and Mn^{2+} in the solution fast generates MnO_x composite, leading to the thick inhomogeneous structure. It is noteworthy that the introduction of Fe sources ($FeSO_4$) for the Fe_2O_3@Fe doped K-birnessite composite effectively results in uniform MnO_x layers covering the nano-sized iron oxide core (Fig. 2d and h).

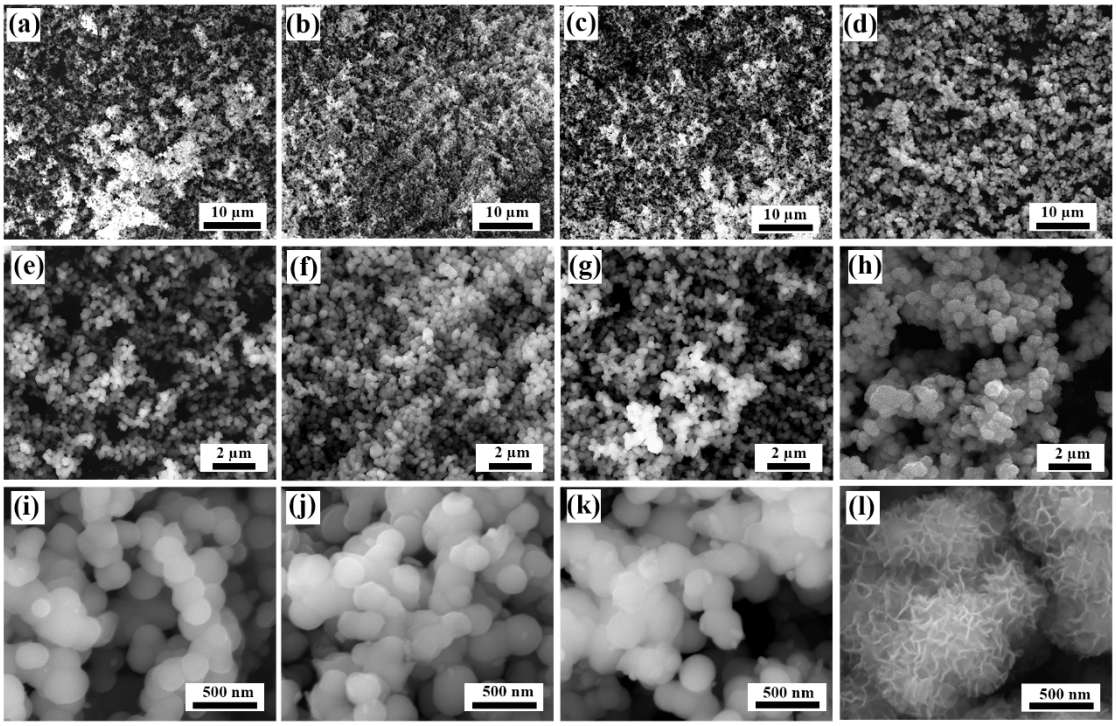

Fig. 2. SEM images of synthetic samples with 30 (a, e and i), 60 (b, f and j), 90 (c, g and k) and 180 (d, h and l) min's growth time, respectively. (m-p) SEM-EDS mapping of elemental K (m), Fe (n), Mn (o) and O (p) for synthetic samples with 180 min growth time corresponding to Fig. 2l.

TEM images of the synthetic samples with different growth times (30, 60, 90 and 180 min) are shown in Fig. 3. The low-magnification TEM images (Fig. 3a-d) show clearly the morphology evolution of samples with different growth time, a process that the initial spherical shape slowly grows up to stacking spherical nanoplates, which turn to be a uniform flower-like hierarchical structure. The high-resolution TEM images with the growth time of 30 (Fig. 3e) or 60 min (Fig. 3f) show the amorphous structure, in agreement of the XRD patterns (Fig. 1a). The high-resolution TEM image with growth time of 90 min (Fig. 3g) demonstrates a crystalline interplanar spacing with 0.25 nm assigning to the (1 1 0) plane of Fe_2O_3 (JCPDS no. 33-0664), indicating the formation of Fe_2O_3 nanocrystals, which is also confirmed by previous analysis (Fig. 1a and Eq. 3). When the growth time is 180 min, the high-resolution TEM image

of (Fig. 3h) shows a homogenous flower-like structure. In comparison, TEM images of pure K-birnessite (Fig. S9) show a disordered thick hierarchical structure, further confirming that the successful iron doping. The d-spacing of lattice fringes of Fe_2O_3@Fe doped K-birnessite is estimated to be 0.66 nm, smaller than the standard value (0.705 nm) of (0 0 1) plane of birnessite (JCPDS no. 80-1098) which is also found in the pure K-birnessite (Fig. S9b) with 180 min's growth time. This phenomenon is likely attributed to the loss of water molecule in the composite interlayer during the TEM measurement [49, 50]. In addition, no obvious lattice fringes of Fe_2O_3 in the layer surface of composite are observed, while STEM-EDS mapping images (Fig. 3i-m) show the uniform distribution of K, Fe, Mn and O elements. This observation confirms iron doping in the composite and a slight amount of Fe_2O_3 nanocrystals are embedded in the core of Fe_2O_3@Fe doped K-birnessite composite. Moreover, the elemental compositions are further examined by ICP-OES measurement, the chemical formulas of Fe_2O_3@Fe doped K-birnessite and pure K-birnessite composite are determined to be $K_{0.14}Fe_{0.33}Mn_{0.53}O_x$ (H_2O) and $K_{0.27}Mn_{0.73}O_x$ (H_2O), respectively. Thus, the hypothetical structure of flower-like Fe_2O_3@Fe doped K-birnessite composite (Scheme 1) is composed of edge-shared Fe doping 2D manganese oxide octahedra with interstitial cations/molecules (K^+, H_2O) to balance the overall charge of the layers originating from inclusion of Mn^{2+}, Mn^{3+} or Fe^{3+} sites into the Mn^{4+} sheets, and internal Fe_2O_3 nanocrystals.

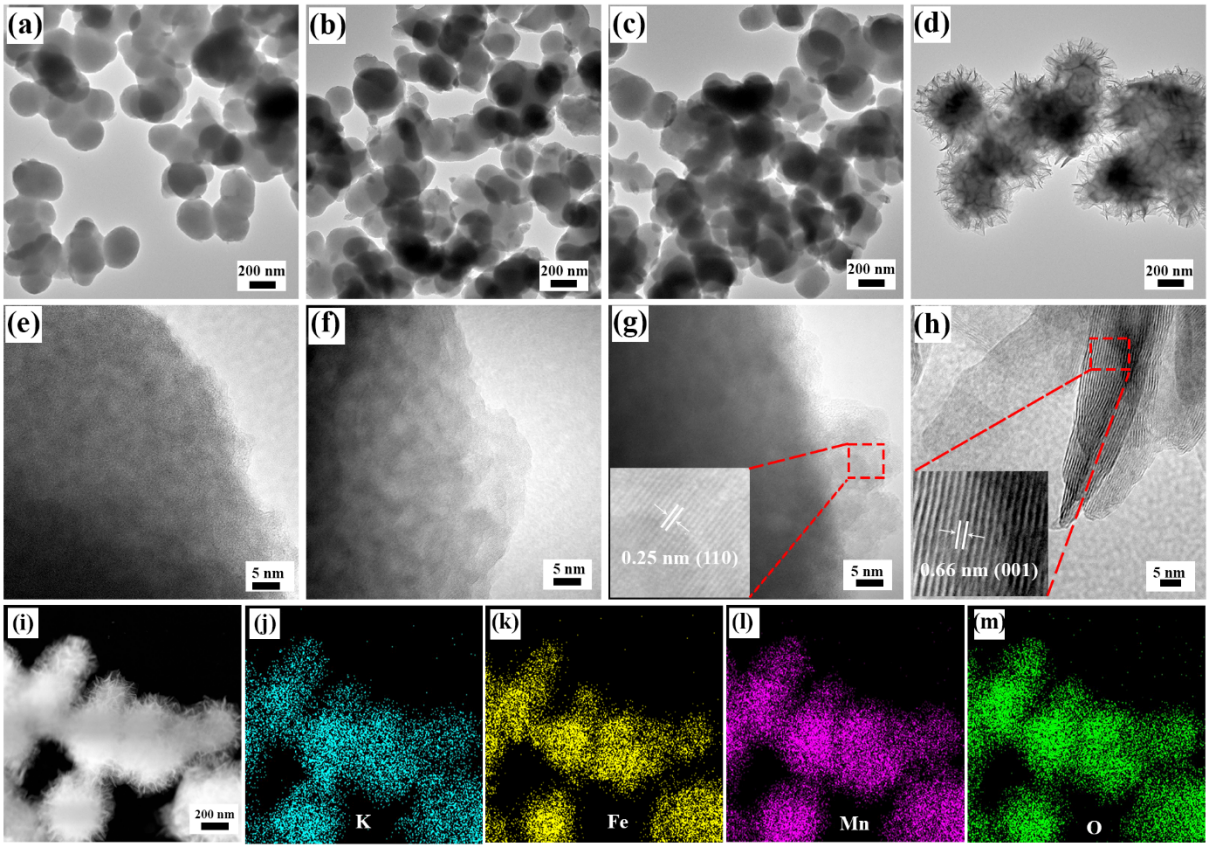

Fig. 3. TEM images of synthetic samples with 30 (a), 60 (b), 90 (c) and 180 (d) min growth time, respectively. High-resolution TEM images of synthetic samples with 30 (e), 60 (f), 90 (g) and 180 (h) mins growth time, respectively. (i-m) HAADF STEM image (i) and corresponded STEM-EDS mapping of elemental K (j), Fe (k), Mn (l) and O (m) for synthetic samples with a 180 min growth time.

3.3. Crystalline and morphology evolution with different reactive temperatures and stoichiometric ratios.

The influential factors, i.e. reactive temperature and stoichiometric ratio of $KMnO_4/FeSO_4{\cdot}7H_2O$, affecting the formation of flower-like Fe_2O_3@Fe doped K-birnessite composite have been further investigated. Reactive temperatures either lower or higher than 140°C are evaluated. When using 120 °C for 180 min, the samples (Fig. 4a, c and e) show a nanoplate morphology, indicating that the low reactive temperature leads to the sluggish

formative rate of flower-like structure. 160 °C for 180 min (Fig. 4b, d and f) results in samples showing larger size with thicker layers than the samples obtained at 140 °C, revealing the high reactive temperature causing the continuous growth of particles and layers. In addition, the samples fabricated at the optimal temperature condition (140 °C, 180 min) with autoclave reaction (Fig. S10) do not show a flower-like structure, emphasizing the role of microwave power for the fast formation of flower-like hierarchical-layer structure.

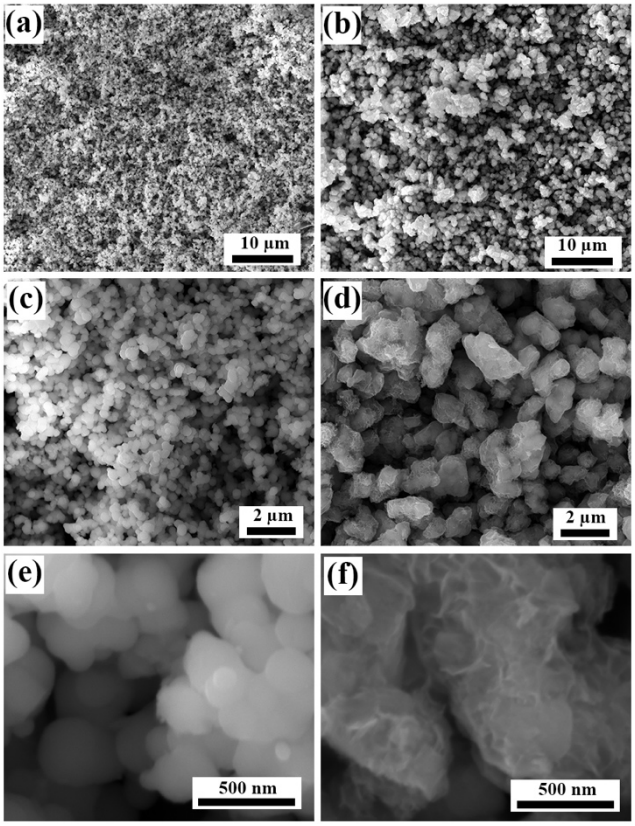

Fig. 4. SEM images of synthetic samples at 120 °C (Fig. 4a, c and e) and 160 °C (Fig. 4b, d and f) by 180 min microwave reaction.

The effect of the mass ratio of $KMnO_4$ and $FeSO_4 \cdot 7H_2O$ (140 °C, 180 min) upon the sample morphology is systematically investigated by XRD and SEM measurement. When the mass ratio ($KMnO_4$/$FeSO_4 \cdot 7H_2O$) is 0.2/0.2, the obtained samples are confirmed by the XRD with main peaks (Fig. 5a) matching well with that of Fe_2O_3 (JCPDS no. 33-0664), with a stacked

spherical shape (Fig. 5d, g and j). The vanish of MnO_x signal in the XRD pattern (Fig. 5a) is mainly due to the complete transform of MnO_4^- to Mn^{2+} due to the enough Fe^{2+} in the reactive process, thus the generated Mn^{2+} dissolves in the solution. When the mass ratio is 0.2/0.4, the samples display (Fig. 5b) the Jarosite XRD patterns ($KFe_3(SO_4)_2(OH)_6$, JCPDS no. 22-0827) and a mixed structure of nanoplates and nanospindles (Fig. 5e, h and k). For a mass ratio of 0.2/0.05, the XRD pattern (Fig. 5c) and SEM images (Fig. 5f, i and l) of synthetic samples show similar results to the composite obtained from 0.2/0.1, but with a much lower yield (ca. 60 mg) than that (ca. 120 mg) of Fe_2O_3@Fe doped K-birnessite composite (0.2/0.1). Accordingly, Fe_2O_3@Fe doped K-birnessite with an optimal ratio 0.2/0.1 is selected due to the largest yield and obtaining a homogenous flower-like structure with a strong interaction between internal Fe_2O_3 nanocrystals and outer hierarchal MnO_x layers, originating from the comparable ionic radii between Mn and Fe cations [29, 33].

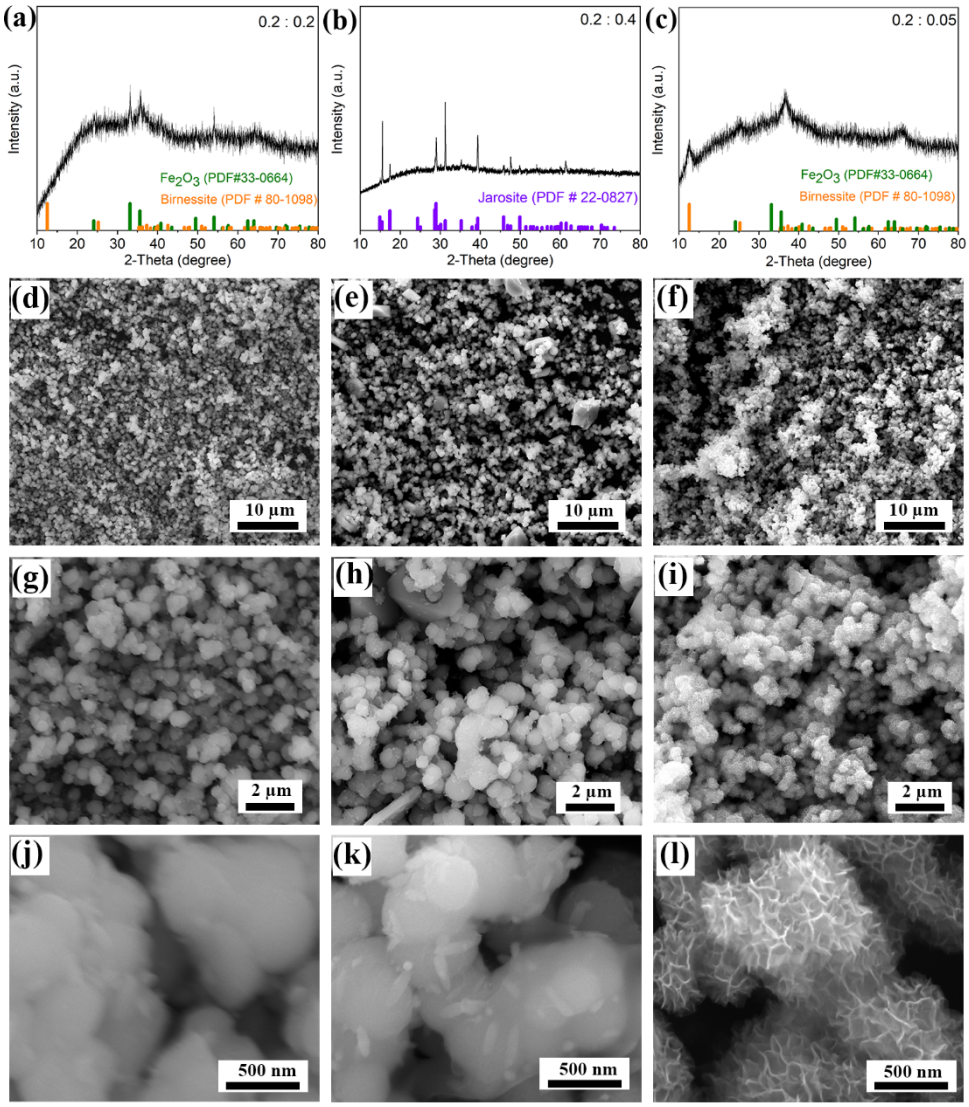

Fig. 5. XRD patterns and SEM images of synthetic samples with different mass ratios of $KMnO_4$ and $FeSO_4 \cdot 7H_2O$ including 0.2: 0.2 (a, d, g and j), 0.2: 0.4 (b, e, h and k) and 0.2: 0.05 (c, f, i and l) at 140 °C for 180 min.

3.4. Lithium ion performance.

In order to investigate the lithium ion storage performance of Fe_2O_3@Fe doped K-birnessite and pure K-birnessite composites, half-cell configurations are assembled with active materials as the working electrodes and lithium foils as the counter electrodes. Fig. 6a shows cyclic voltammograms (CVs) of the first five cycles for Fe_2O_3/Fe doped K-birnessite composite in the

voltage range of 0.01-3.0 V at a scan rate of 0.1 mV s^{-1}. The small cathodic peaks at ca. 2.68 and 1.48 V in the first cycle are mainly attributed to the lithium intercalation in the iron doping K-birnessite layers and the internal Fe_2O_3 with the generation of solid electrolyte interface (SEI), formation of $LiMnO_X$ and $Li_yFe_2O_3$. A broad peak at ca. 0.50 V and a sharp peak at ca. 0.19 V in the cathodic scan are mainly assigned to the conversion of Fe^{3+} to Fe^0 and the generation of Li_2O and metallic Mn, respectively [12, 29]. The obvious oxidation peak at ca. 1.16 V and slight peak at ca. 1.56 V are corresponded to the electrochemical oxidative reaction of metallic Mn and Fe^0, respectively. It is noteworthy that Fe could maintain as zero-valent iron nanoparticles during the reduction/oxidation reaction of K-birnessite typed MnO_x due to the reduction of Fe^{3+} to Fe^0 occurs early during the discharge scan, while oxidation of metallic iron takes place in the higher potential during the charge scan. The existence of zero-valent iron could efficiently improve the integral conductivity of MnO_x with fast electron transfer diffusion for good electrochemical performance [33]. After initial scans, the broad cathodic and anodic peaks gradually shift and become stable at ca. 0.15 and 1.35 V, respectively. The slight voltage shifts are attributed to the polarization stemming from the electrode resistance [51]. In comparison, the CVs of pure K-birnessite composite without Fe doping (Fig. S11) show a cathodic peak at ca. 0.19 V and an anodic peak at ca. 1.21 V after the initial cycle. The similar stable cathodic and anodic peak positions in the CVs indicate the main redox reaction is due to the reaction of MnO_x and Li^+ for lithium ion storage. Besides, previous reports show the stable cathodic peak of Fe_2O_3 for lithium ion storage after initial scan is at ca. 0.75 V [27, 29]. The weak cathodic peak assigning to Fe_2O_3 in CVs of Fe_2O_3@Fe doped K-birnessite composite indicates a slight existence of Fe_2O_3 nanocrystals. These results indicate the abundant majority of lithium storage capability of the Fe_2O_3@Fe doped K-birnessite composite is originated from the iron doping K-birnessite layers. The Galvanostatic discharge/charge (GDC)

profiles of Fe_2O_3@Fe doped K-birnessite composite with the first five cycles at a current density of 100 mA g^{-1} are shown in Fig. 6b. In the initial cycle, the gradual slope in the region of 1.0-0.45 V is associated with the broad cathodic wave starting from 1.0 V with a peak at ca. 0.50 V, assigning to the conversion of Fe^{3+} to Fe^0. In addition, the platform starting from ca. 0. 43 V for the first discharge profile matches with the cathodic peak with a relatively sharp peak at ca. 0.19 V, corresponding to the generation of Li_2O and metallic Mn, respectively. In subsequent CVs, the platform at ca. 0.50 V in discharge profiles are attributed to the broad cathodic wave ranging from ca. 0.7 to 0.05 V with a peak at ca. 0.15 V. The potential region (0.7-0.05 V) means the main reaction of the formation of Li_2O and metallic Mn occurs in the process, in good agreement with gradual platforms in the discharge profiles. Similar phenomenon is also found in previous reports [33, 52]. The cycling performance of the Fe_2O_3@Fe doped K-birnessite composite at a current density of 100 mA g^{-1} is shown in Fig. 6c. The initial discharge and charge capacities are 1490 and 604 mA h g^{-1}, respectively. The relatively low initial Coulombic efficiency (41 %) are attributed to the escape of crystalline water molecules in the structure of composite (rather than free water), partially irreversible side reaction of the electrode materials with electrolyte and the formation of a SEI film. Then the discharge capacity deceases to 352 mA h g^{-1} after 40 cycles, after which the discharge capacity gradually increases and stabilizes to 742 mA h g^{-1} until 140 cycles, with a Coulombic efficiency of almost 100% after 15 cycles. The phenomenon is believed to the result of a range of activation processes including the long-term activation of electrode materials for structural rearrangement, offering more active sites for lithium storage in the subsequent discharge-charge cycles [5, 18]. Besides, the generation of higher-oxidation-state manganese in the composite by Li_2O oxidation during the charge process and the formation of electrochemically active gel-like films on the surface of Fe_2O_3@Fe doped K-birnessite electrode could improve

efficiently the lithium storage capacity. This is also confirmed by previous reports about manganese-based materials for lithium ion storage [18, 27, 52]. As a control, the pure K-birnessite composite (Fig. 6d) delivers the initial discharge and charge capacity of 1373 and 430 mA h g^{-1} at 100 mA g^{-1}, with a low Coulombic efficiency of 31 %. In addition, the discharge capacity decreases to 311 mA h g^{-1} after 140 cycles. The higher capacity retention for Fe_2O_3@Fe doped K-birnessite is mainly attributed to the Fe doping in the K-birnessite composite decreases the size of particles and provides larger specific surface area for more exposing active sites. Fe_2O_3@Fe doped K-birnessite composite (Fig. S12a) demonstrates capacities of 403, 282, 177, 104 mA h g^{-1} at current densities of 100, 200, 500, 1000 mA g^{-1}, respectively. When the current density is set back to 100 mA g^{-1} after 40 cycles, the capacity retained 346 mA h g^{-1}. As a contrast, the pure K-birnessite composite (Fig. S12b) exhibits capacities of 299, 200, 121, 70 mA h g^{-1} at current densities of 100, 200, 500, 1000 mA g^{-1}, respectively. When the current density is reduced back to 100 mA g^{-1} after 40 cycles, the capacity only recovers to 239 mA h g^{-1}.

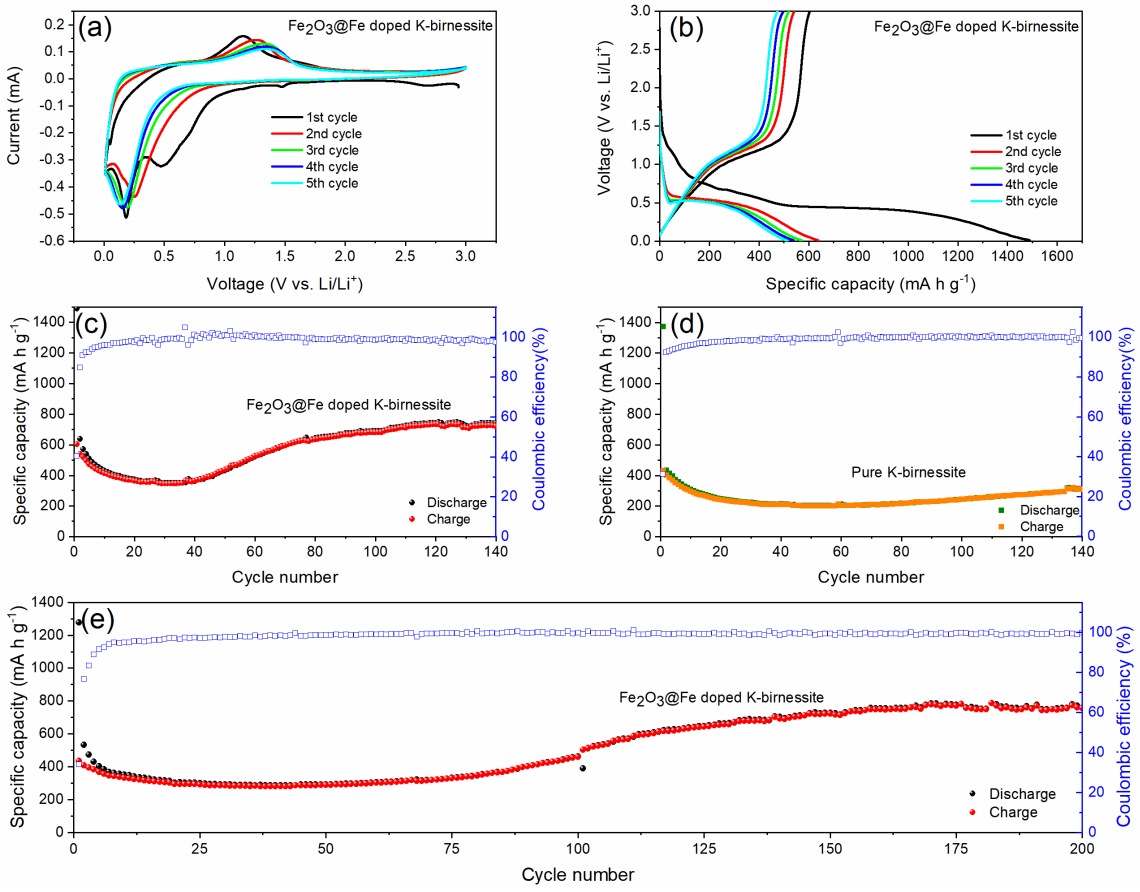

Fig. 6. (a) CVs of the first five cycles for Fe_2O_3@Fe doped K-birnessite with a scan rate of 0.1 mV s^{-1}. (b) Galvanostatic discharge/charge profiles of the first five cycles at a current density of 100 mA g^{-1}. (c, d) Cycling performance of Fe_2O_3@Fe doped K-birnessite (c) and pure K-birnessite (d) composites at a current density of 100 mA g^{-1}. (e) Long-term cycling performance of Fe_2O_3@Fe doped K-birnessite at a current density of 500 mA g^{-1}.

In order to investigate further the cycling performance of Fe_2O_3@Fe doped K-birnessite composite at high current density, Fig. 6e shows the long-term cycling performance of Fe_2O_3/Fe doped K-birnessite at 500 mA g^{-1}. The capacities also demonstrate a long activation process for 39 cycles, then gradually increases and stabilizes to a reversible capacity of 758 mA h g^{-1} after 200 cycles. The Coulombic efficiency is more than 94 % after the first six cycles. In converse, the pure K-birnessite composite (Fig. S13) exhibits interferer irreversible

capacities after only 140 cycles, with a much higher charge capacity than the discharge capacity as a sign of the complete breakdown of active materials on the electrode. Therefore, the introduction of Fe source in the K-birnessite composite could effectively reinforce the flower-like structural stability for good cycling performance. Comparing with previously reported manganese oxide based composites for lithium ion storage (Table S1), the Fe_2O_3@Fe doped K-birnessite composite demonstrates a good electrochemical performance.

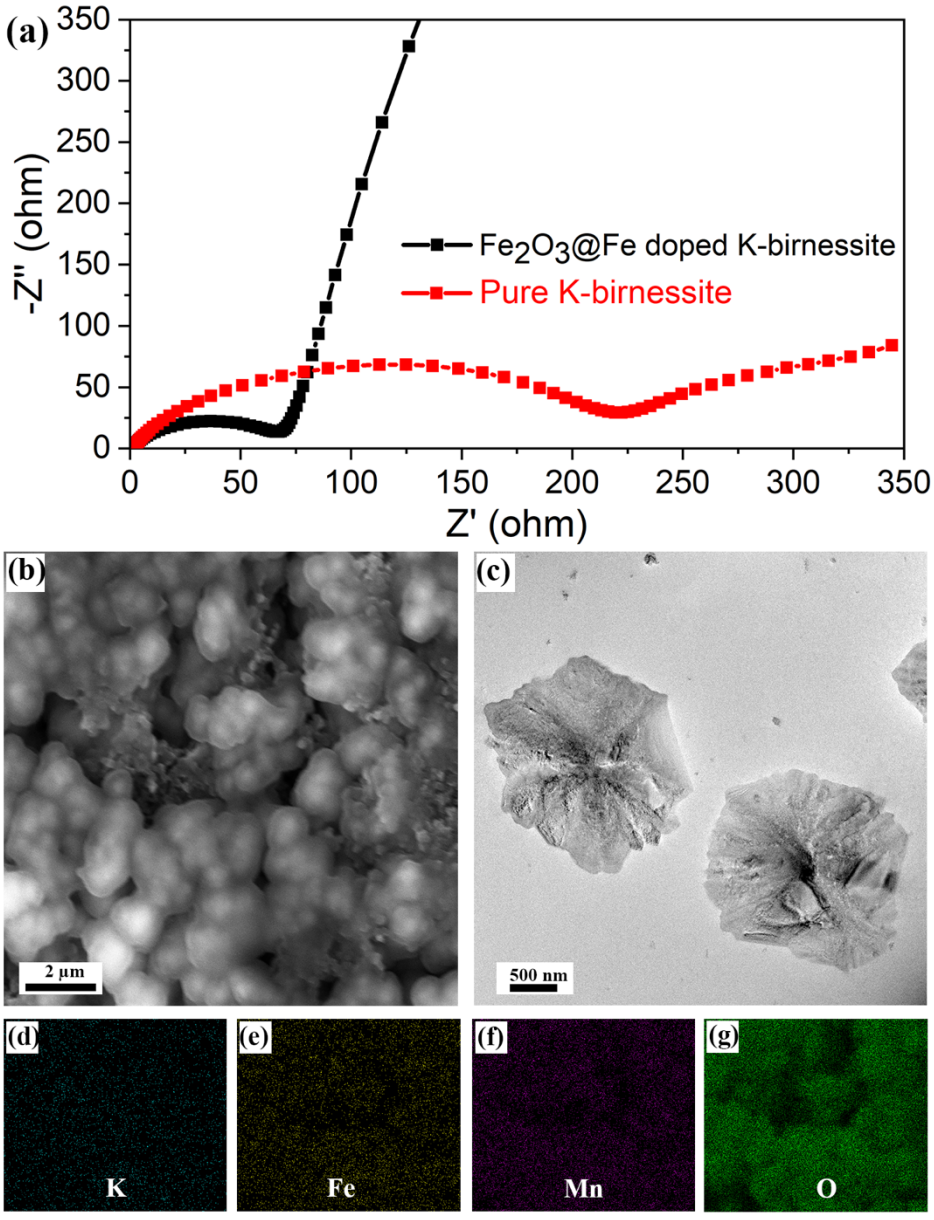

Fig.7. (a) Nyquist plots of Fe_2O_3@Fe doped K-birnessite and pure K-birnessite composites. SEM (b) and TEM (c) images of Fe_2O_3@Fe doped K-birnessite composite based lithium storage material after 140 cycles at 100 mA g^{-1}, (d-g) EDS mapping images correspond to Fig. 7b.

In order to make a good understanding of Fe_2O_3@Fe doped K-birnessite for lithium ion storage performance, electrochemical impedance spectroscopy (EIS) of fresh cells are recorded. Nyquist plots of Fe_2O_3@Fe doped K-birnessite and pure K-birnessite composites are shown in Fig. 7a. Semicircles in high-middle frequency region correspond to the charge-transfer resistance (R_{ct}) through the electrode/electrolyte interfaces. The R_{ct} (52 Ω) of Fe_2O_3@Fe doped K-birnessite is much lower than that of pure K-birnessite composite (210 Ω). The result indicates Fe doping in the K-birnessite composite efficiently improves the overall electrical conductivity and decreases the interface polarization of electrode. Moreover, the Fe_2O_3@Fe doped K-birnessite after testing at 100 mA g^{-1} for 140 cycles has been evaluated by SEM and EDS (Fig. 7b, d-g), which clearly indicate the Fe_2O_3@Fe doped K-birnessite composite stably exists in the electrode. TEM images (Fig. 7c) shows a corresponding flower-like structure, further confirming the structural stability. The reasons for Fe_2O_3@Fe doped K-birnessite composite showing an enhanced lithium-ion storage performance than pure K-birnessite can be summarized as: (1) the monodisperse flower-like Fe_2O_3@Fe doped K-birnessite particles with a high specific surface area provide abundant active sites for lithium insertion/extraction. (2) The synergetic effects of K-birnessite type MnO_x and Fe_2O_3 promise the improved lithium capacity with a strong interaction between MnO_x and Fe_2O_3, originating from the comparable ionic radii between Mn and Fe cations [29, 33]. (3) iron doping in the K-birnessite typed MnO_x not only facilitates the bulk conductivity and promotes the electron transfer kinetics, but also provides extra active sites from the defects of iron doping. There

results guarantee flower-like Fe_2O_3@Fe doped K-birnessite composite demonstrate a good electrochemical performance and can be an alternative anode material for LIBs.

4. Conclusions

Flower-like Fe_2O_3@Fe doped K-birnessite composite has been successfully fabricated using one-pot microwave reaction, and the crystalline and morphology evolution of Fe_2O_3@Fe doped K-birnessite composite related to the microwave reactive durations, reactive temperatures and stoichiometric ratios have been systematically investigated. When the designed composites are used for lithium ion storage, the comparison study indicates that the hybrid composite exhibits superior performance regarding to capacity and operational stability than that of the pure K-birnessite. Synergetic effects from the flower-like structure consisting of internal slight Fe_2O_3 nanocrystals and outer hierarchal iron doped K-birnessite type MnO_x layers with strong interaction and optimized electronic structure are believed to be responsible for the improved electrochemical behaviors. The structural design and promising performance of Fe_2O_3@Fe doped K-birnessite composite will ensure the composite could be a promising anode material of LIBs for potential practical applications and inspire the development of lithium ion batteries.

Declaration of interests

The authors declare no competing financial interest.

Acknowledgments

Finance support from Chinese Scholarship Council (201706220080) for W.H., Department of Science and Technology of Shandong Province (2018JMRH0211, ZR2019MEM052, 2019TSLH0101 and ZR2018ZB0105), the Fundamental Research Funds of Shandong University

(2017JC042 and 2017JC010). The Danish Council for Independent Research for the YDUN project (DFF 4093-00297) to J.Z., H. C. Ørsted COFUND fellowship for X. X.

References

[1] M.S. Dresselhaus, I.L. Thomas, Nature, 414 (2001) 332-337.
[2] B. Dunn, H. Kamath, J.-M. Tarascon, Science, 334 (2011) 928-935.
[3] M. Armand, J.-M. Tarascon, Nature, 451 (2008) 652-657.
[4] J.W. Choi, D. Aurbach, Nat. Rev. Mater., 1 (2016) 16013.
[5] W. Huang, S. Li, X. Cao, C. Hou, Z. Zhang, J. Feng, L. Ci, P. Si, Q. Chi, ACS Sustainable Chem. Eng., 5 (2017) 5039-5048.
[6] G.E. Blomgren, J. Electrochem. Soc., 164 (2017) A5019-A5025.
[7] Z. Liu, Q. Yu, Y. Zhao, R. He, M. Xu, S. Feng, S. Li, L. Zhou, L. Mai, Chem. Soc. Rev., 48 (2019) 285-309.
[8] H. Shangguan, W. Huang, C. Engelbrekt, X. Zheng, F. Shen, X. Xiao, L. Ci, P. Si, J. Zhang, Energy Storage Mater., 18 (2019) 114-124.
[9] B. Wang, J. Ryu, S. Choi, X. Zhang, D. Pribat, X. Li, L. Zhi, S. Park, R.S. Ruoff, ACS Nano, 13 (2019) 2307-2315.
[10] P. Poizot, S. Laruelle, S. Grugeon, L. Dupont, J.-M. Tarascon, Nature, 407 (2000) 496-499.
[11] Y. Lu, L. Yu, X.W.D. Lou, Chem, 4 (2018) 972-996.
[12] W. Huang, X. Xiao, C. Engelbrekt, M. Zhang, S. Li, J. Ulstrup, L. Ci, J. Feng, P. Si, Q. Chi, Mater. Chem. Front., 1 (2017) 1185-1193.
[13] L. Zhou, K. Zhang, Z. Hu, Z. Tao, L. Mai, Y.-M. Kang, S.-L. Chou, J. Chen, Adv. Energy Mater., 8 (2018) 1701415.
[14] Q. Li, Y. Feng, P. Wang, R. Che, Nanoscale, 11 (2019) 5080-5093.
[15] H. Sun, Y. Zhao, K. Mølhave, M. Zhang, J. Zhang, Nanoscale, 9 (2017) 14431-14441.
[16] M. Zheng, H. Tang, L. Li, Q. Hu, L. Zhang, H. Xue, H. Pang, Adv. Sci., 5 (2018) 1700592.
[17] L. Ji, Z. Lin, M. Alcoutlabi, X. Zhang, Energy Environ. Sci., 4 (2011) 2682-2699.
[18] Y. Chu, L. Guo, B. Xi, Z. Feng, F. Wu, Y. Lin, J. Liu, D. Sun, J. Feng, Y. Qian, Adv. Mater., 30 (2018) 1704244.
[19] H. Li, P. Balaya, J. Maier, J Electrochem. Soc., 151 (2004) A1878-A1885.
[20] J. Gao, M.A. Lowe, H.D. Abruna, Chem. Mater., 23 (2011) 3223-3227.
[21] Q. Fan, M.S. Whittingham, Electrochem. Solid-State Lett., 10 (2007) A48-A51.
[22] X.Q. Yu, Y. He, J.P. Sun, K. Tang, H. Li, L.Q. Chen, X.J. Huang, Electrochem. Commun., 11 (2009) 791-794.
[23] H. Wang, L.-F. Cui, Y. Yang, H. Sanchez Casalongue, J.T. Robinson, Y. Liang, Y. Cui, H. Dai, J. Am. Chem. Soc., 132 (2010) 13978-13980.
[24] J.-G. Wang, D. Jin, R. Zhou, X. Li, X.-r. Liu, C. Shen, K. Xie, B. Li, F. Kang, B. Wei, ACS Nano, 10 (2016) 6227-6234.
[25] Z. Yang, J. Lv, H. Pang, W. Yan, K. Qian, T. Guo, Z. Guo, Sci. Rep., 5 (2015) 17473.
[26] J.-Y. Liao, D. Higgins, G. Lui, V. Chabot, X. Xiao, Z. Chen, Nano Lett., 13 (2013) 5467-5473.
[27] D. Wang, Y. Wang, Q. Li, W. Guo, F. Zhang, S. Niu, J. Power Sources, 393 (2018) 186-192.
[28] M. Kundu, G. Singh, A.M. Svensson, New J. Chem., 43 (2019) 1257-1266.
[29] C. Zeng, W. Weng, T. Lv, W. Xiao, ACS Appl. Mater. Interfaces, 10 (2018) 30470-30478.
[30] J. Kang, A. Hirata, L. Kang, X. Zhang, Y. Hou, L. Chen, C. Li, T. Fujita, K. Akagi, M. Chen, Angew. Chem. Int. Ed., 52 (2013) 1664-1667.
[31] Z. Ye, T. Li, G. Ma, Y. Dong, X. Zhou, Adv. Funct. Mater., 27 (2017) 1704083.
[32] A. Ogata, S. Komaba, R. Baddour-Hadjean, J.-P. Pereira-Ramos, N. Kumagai, Electrochim. Acta, 53 (2008) 3084-3093.
[33] Y. Ma, C. Fang, B. Ding, G. Ji, J.Y. Lee, Adv. Mater., 25 (2013) 4646-4652.

[34] J.-S. Schanche, Mol. Divers., 7 (2003) 291-298.
[35] R. Morschhäuser, M. Krull, C. Kayser, C. Boberski, R. Bierbaum, P.A. Püschner, T.N. Glasnov, C.O. Kappe, Green Process. Synth., 1 (2012) 281-290.
[36] K.S.S. Jensen, H. Sun, R.M.L. Werchmeister, K. Mølhave, J. Zhang, Curr. Opin. Electrochem., 4 (2017) 124-132.
[37] X. Chen, G. Wu, J. Chen, X. Chen, Z. Xie, X. Wang, J. Am. Chem. Soc., 133 (2011) 3693-3695.
[38] B. Ming, J. Li, F. Kang, G. Pang, Y. Zhang, L. Chen, J. Xu, X. Wang, J. Power Sources, 198 (2012) 428-431.
[39] W. Guo, W. Sun, L.-P. Lv, S. Kong, Y. Wang, ACS Nano, 11 (2017) 4198-4205.
[40] J. Yan, P. Li, Y. Ji, H. Bian, Y. Li, S.F. Liu, J. Mater. Chem. A, 5 (2017) 21478-21485.
[41] A.P. Grosvenor, B.A. Kobe, M.C. Biesinger, N.S. McIntyre, Surf. Interface Anal., 36 (2004) 1564-1574.
[42] X. Wang, L. Mei, X. Xing, L. Liao, G. Lv, Z. Li, L. Wu, Appl. Catal. B., 160 (2014) 211-216.
[43] W. Gu, G. Lv, L. Liao, C. Yang, H. Liu, I. Nebendahl, Z. Li, J. Hazard. Mater., 338 (2017) 428-436.
[44] H. Yin, F. Liu, X. Feng, T. Hu, L. Zheng, G. Qiu, L.K. Koopal, W. Tan, Geochim. Cosmochim. Acta, 117 (2013) 1-15.
[45] Z. Li, A. Gu, Z. Lou, J. Sun, Q. Zhou, K.Y. Chan, J. Mater. Sci., 52 (2017) 4852-4865.
[46] R. Chen, P. Zavalij, M.S. Whittingham, Chem. Mater., 8 (1996) 1275-1280.
[47] J. Zhu, S. Tang, H. Xie, Y. Dai, X. Meng, ACS Appl. Mater. Interfaces, 6 (2014) 17637-17646.
[48] X. Wang, Y. Li, Chem. Eur. J., 9 (2003) 300-306.
[49] Y. Li, Y. Li, A. Pei, K. Yan, Y. Sun, C.-L. Wu, L.-M. Joubert, R. Chin, A.L. Koh, Y. Yu, J. Perrino, B. Butz, S. Chu, Y. Cui, Science, 358 (2017) 506-510.
[50] A. Gao, M. Li, N. Guo, D. Qiu, Y. Li, S. Wang, X. Lu, F. Wang, R. Yang, Adv. Eng. Mater., (2018) 1802739.
[51] T. Jiang, S. Zhang, X. Qiu, W. Zhu, L. Chen, Electrochem. Commun., 9 (2007) 930-934.
[52] X. Hu, X. Lou, C. Li, Q. Yang, Q. Chen, B. Hu, ACS Appl. Mater. Interfaces, 10 (2018) 14684-14697.

1

Table of contents

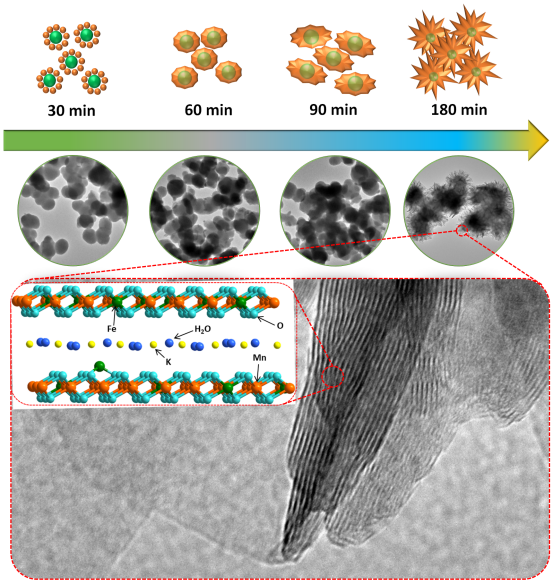

2